Transport coefficients of layered TiS_3

Robert Biele[1,*] and Roberto D'Agosta[2,†]

[1]*Institute for Materials Science and Max Bergmann Centre of Biomaterials, Dresden University of Technology, 01069 Dresden, Germany*

[2]*Nano-bio spectroscopy group, Advanced Polymers and Materials: Physics, Chemistry and Technology, Chemistry Faculty, Universidad del Pais Vasco (UPV/EHU), 20018 San Sebastian, Spain and Ikerbasque, Basque Foundation for Science, Plaza de Euskadi 5, E-48009 Bilbao, Spain*

(Received 3 September 2021; revised 2 December 2021; accepted 4 January 2022; published 21 January 2022)

We investigate the electrical and thermal transport coefficients of an emergent transition metal trichalcogenide, namely, TiS_3. We implement an accurate description of the electron-phonon coupling and thus of the energy dependence of the relaxation time, which goes beyond the commonly used approximations. We find that standard calculation methods fail in accurately describing the thermoelectric transport properties of TiS_3 and one needs to go beyond standard approximations to correctly investigate the thermoelectric performance of TiS_3 and other 2D materials. By applying state-of-the-art *ab initio* methods, we conclude that TiS_3 stands as a potential candidate for thermoelectric applications.

DOI: 10.1103/PhysRevMaterials.6.014004

I. INTRODUCTION

The discovery of graphene brought the investigation of two-dimensional (2D) materials to the forefront of scientific research [1,2]. The reason for this evolution lies in the potential applications that these materials find in technology. Indeed, 2D materials show extraordinary electronic, thermal, and elastic properties dramatically different from their bulk counterpart. In the family of 2D materials, one class, the transition metal tri-chalcogenides (TMTC), is currently investigated for their outstanding optical and transport properties, some of which are related to the intrinsic anisotropy of their atomic structure. Moreover, some of these properties can be controlled through external deformation, thus making TMTC an extremely ductile playground to explore the properties of 2D materials. TMTC lack the exciting topological properties of other materials like graphene or MoS_2, but their outstanding optical response makes them suitable for building up novel transistors or sensors [3–14].

Among this class, the first material that attracted the interest of the scientific community is TiS_3 [3–10,15]. In its stable configuration, at room temperature, it forms layers of 8 atoms (2 Ti and 6 S), of which 4 S belong to the surface, and 2 are internal to the Ti atoms (see Fig. 1). The layers are kept together by weak van der Waals (vdW) forces. The unit cell of monolayer TiS_3 presents a strong anisotropy with one edge shorter than the other. Our calculation gives $|\mathbf{a}| = 4.99$ Å, $|\mathbf{b}| = 3.40$ Å, $|\mathbf{c}| = 8.90$ Å, $\beta = 97.3°$, where β is the angle between a and c, in reasonable agreement with the experimental results [$|\mathbf{a}| = 4.973(0)$ Å, $|\mathbf{b}| = 3.433(0)$ Å, $|\mathbf{c}| = 8.714(0)$ Å, $\beta = 97.74(0)°$] [3]. In contrast, for the monolayer, we obtain the values $|\mathbf{a}| = 5.03$ Å and $|\mathbf{b}| = 3.42$ Å. Besides the interest as material for optical applications, TiS_3 has been investigated as a material for electronics, optoelectronics, and thermoelectricity. For some of these uses, one needs to evaluate both the phononic and electronic transport coefficients.

In general, the electronic transport properties are affected by scattering events of electrons with phonons, and hence one needs to carefully consider the so-called electron-phonon (e–p) interaction. The necessity of an accurate evaluation of the transport coefficients has been pointed out also for other materials, like, e.g., phosphorene [16–18], $ZrSe_3$ [8]. Indeed, we expect that the correction to the relaxation time applies to the whole family of 2D materials. The methods we present in the following are easily applicable to other 2D materials, and we expect our results to be of general interest and application. Recently, e–p interaction has received much attention, especially in the *ab initio* community. The constant increase of the quality of the codes and the computational power makes the first-principle evaluation of the e–p coupling possible. From the e–p coupling, we can evaluate the electron relaxation time considering one of its significant contributions, namely the scattering with phonons. In the past, the standard approximation was to consider the electron relaxation time τ as a constant that was evaluated either as a fitting parameter, via the use of the simple Drude's formula if the conductance was somewhat known, or via some other sophisticated models, which however completely neglected the energy dependence of τ.

In this paper, we will focus on calculating the thermoelectric response of TiS_3 as both bulk and monolayer. (See Fig. 1.) We aim at calculating $\tau(\omega)$, as a function of the energy ω, and all the transport coefficients along the unit-cell axis. We will compare two methods to evaluate τ: one is in principle exact, the other an approximation, known as e–p averaged (EPA) approximation and has the advantage of reproducing the correct transport properties while reducing the computational

*robert.biele@tu-dresden.de
†roberto.dagosta@ehu.es

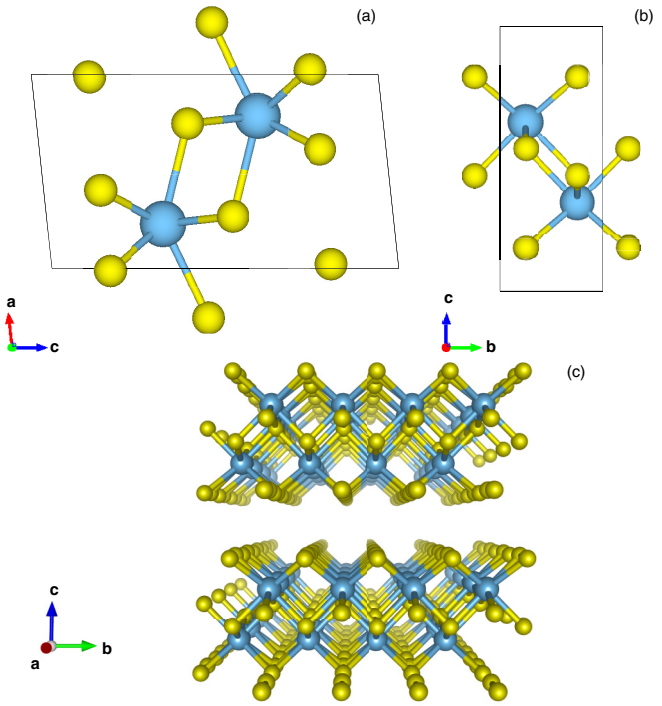

FIG. 1. Atomic structure of TiS_3. (a) Projection along the **b** axis. (b) Projection along the **a** axis. (c) Prospective view showing two layers of the bulk structure. The **a** axis is oriented outside the page. We plot in yellow the sulphur atoms, while in blueish the titanium atoms. The figure was made with VESTA [19].

cost of the exact calculation [20]. Recently we became aware of another approximation, dubbed MRTA, which might overcome the limitations of the CRT approximation, without the computational cost of the full EPW calculation [21]. A direct comparison between the MRTA and the EPA/EPW lies outside the scope of this paper.

II. THEORY AND METHODS

Our starting point is the Boltzmann transport equation (BTE) for the electronic single-particle distribution function $f_{n\mathbf{k}}$, where n is the band index and $\mathbf{k}$ its momentum. From the solution of the BTE, one can obtain all the transport coefficients through a relatively simple integration in the first Brillouin zone. A parameter entering the BTE is the electron relaxation time $\tau_{n\mathbf{k}}$. Different scattering events determine the relaxation time, but it is mostly dominated by electron-electron (e–e) and e–p scattering in clean materials.

In general, we get the electron relaxation time for e–p scattering in the form

$$\begin{aligned}\tau_{n\mathbf{k}}^{-1}(T,\mu) = \frac{\Omega}{(2\pi)^2\hbar}\sum_{m,v}\int d\mathbf{q}|g_{mnv}(\mathbf{k},\mathbf{q})|^2 \\ \times\left\{\left[n^0_{v\mathbf{q}}+f^0_{m\mathbf{k}+\mathbf{q}}\right]\delta(\epsilon_{n\mathbf{k}}-\epsilon_{m\mathbf{k}+\mathbf{q}}+\hbar\omega_{\mathbf{q}v}) \right. \\ \left. +\left[n^0_{v\mathbf{q}}+1-f^0_{m\mathbf{k}+\mathbf{q}}\right] \right. \\ \left. \times\,\delta(\epsilon_{n\mathbf{k}}-\epsilon_{m\mathbf{k}+\mathbf{q}}-\hbar\omega_{\mathbf{q}v})\right\}, \end{aligned} \tag{1}$$

where Ω is the volume of the Brillouin zone (BZ), g_{mnv} are the matrix elements of the e–p interaction between the states m and n for the electrons and v for the phonon; n^0 is the Bose-Einstein phonon distribution at a given temperature T, f^0 the Fermi distribution at the same temperature and chemical potential μ, ϵ is the electronic energy (depending on the band index n and momentum k), and ω is the phonon frequency. Generally speaking, the e–p matrix elements can be obtained from density-functional perturbation theory calculations [22].

The thermoelectric performance of a material is usually defined in terms of its figure of merit ZT [23,24]. ZT is further expressed as

$$ZT = \frac{S^2\sigma}{\kappa}T = \frac{S^2\sigma}{\kappa_{\rm lat}+\kappa_{\rm el}}T, \tag{2}$$

where S is the Seebeck's coefficient, σ the electrical conductance, κ the overall thermal conductance (that is usually split into its phonon $\kappa_{\rm lat}$ and electron $\kappa_{\rm el}$ contributions). It is therefore clear that the evaluation of ZT requires the knowledge of both electron and phonon transport properties. Generally, the figure of merit of a good thermoelectric material ranges about 1, with the largest reproducible values obtained are above 2. Moreover, ZT strongly depend on the working temperature T.

In the linear response regime [23,25], from the electronic band structure, one evaluates the transport coefficients, for a charge q,

$$L^n_{\alpha,\beta}(\mu,T) = q^2\int d\epsilon g_{\alpha,\beta}(\epsilon,T)(\epsilon-\mu)^n\left(-\frac{\partial f^0}{\partial\epsilon}\right) \tag{3}$$

where $g(\epsilon,T)$ is given by

$$g_{\alpha,\beta}(\epsilon,T) = \sum_{n\in{\rm CB}}\int\frac{d\mathbf{k}}{(2\pi)^3}\delta(\epsilon-\epsilon_{n,\mathbf{k}})v_{n\mathbf{k},\alpha}v_{n\mathbf{k},\beta}\tau_{n\mathbf{k}}, \tag{4}$$

thus the electronic transport coefficients are obtained from the coefficients L,

$$\sigma = L^0, \quad S = \frac{1}{qT}\frac{L^1}{L^0}, \quad \kappa = \frac{1}{q^2T}\left(L^2-\frac{(L^1)^2}{L^0}\right). \tag{5}$$

In the above expression equation (4), $v_{n,\mathbf{k}} = \partial\epsilon_n/\partial\mathbf{k}$ are the pseudo-velocities calculated from the electronic band structure. In principle, the transport coefficients, Eqs. (5), are tensors that retain the underlying anisotropic structure of the materials. For two-dimensional materials, it makes sense to consider only the in-plane components of these tensors.

Usually, the evaluation of the relaxation time is performed at different levels of approximation [26]. The crudest, the constant relaxation time (CRT) approximation, neglects all energy dependence in τ and replaces it with a constant that is evaluated either from empirical data (for example, from the Drude's formula for the electrical conductance) or through simplified models as the deformation potential approximation [27–29] or Allen's formalism [30,31]. Such an approach could be sufficient for simple metals or those occasions where the relaxation time has a lesser impact (for example, in evaluating Seebeck's coefficient). In this paper, we will investigate how equation (1) can be evaluated numerically from first principles for the case study of TiS_3. We will use the code EPW [32,33] for this aim. Also, we will make use of the so-called EPA [20] approximation that turns the demanding integral over

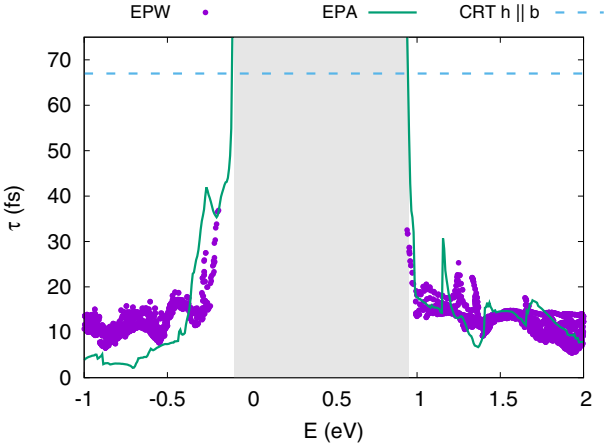

FIG. 2. Relaxation time for the monolayer TiS_3 in the CRT, EPW, and EPA approximations vs the electron energy in eV. The shaded area represents the band gap.

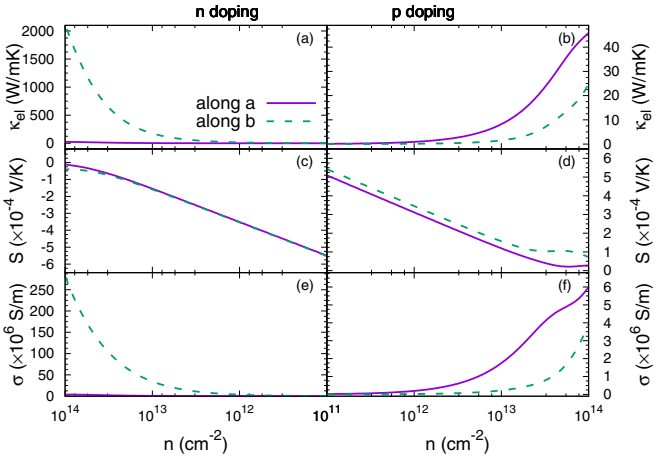

FIG. 3. Electron and hole transport coefficients for the monolayer TiS_3 evaluated in the CRT approximation. Panes (a) and (b) thermal conductance κ_{el} along different direction and doping, respectively. Panes (c) and (d) the Seebeck's coefficient S along different direction and doping, respectively. Panes (e) and (f) the electrical conductance σ along different direction and doping, respectively.

momentum in Eq. (1) into an integration over energy. This step is done by replacing quantities that depend on momentum with their energy-dependent averages. As a result, EPA allows for a faster evaluation of the relaxation time and can be easily combined with a standard numerical tool for the solution of the BTE.

III. RESULTS AND DISCUSSION

We begin with investigating the transport properties of single-layer TiS_3, which can be exfoliated from the bulk structure since the vdW forces between the layers are relatively weak.

In Fig. 2, we plot τ calculated in the EPA and EPW approximations as a function of the energy. The EPW has been converged over different grids of q points, up to a dense 512×512 grid. The grey area represents the band gap, and τ diverges when the energy gets close to the band edges. We see that the EPA approximate the EPW calculation quite well in this energy window. The agreement improves by increasing the number of k points, but decreases at high energies. However, for linear response transport, we are only interested in energies close to the band edges. For each value of the energy E, the EPW calculation gives the scattering time for each associated momentum corresponding to that energy. Here, we pruned some of those points to make the plot readable. We conclude that the EPA provides an accurate description of the scattering time over the range of energies we investigated in this paper.

In the same Fig. 2, we report the relaxation time in the CRT approximation for hole propagating along the **b** axis (about 67 fs). It is clear that CRT overestimates this relaxation time, especially far away from the band edges. Moreover, the relaxation times along the other direction and for both electrons and holes are much larger.

We then calculated the transport coefficients for the ML both in the CRT and EPA approximation at room temperature (300 K). In Fig. 3 we report the electron thermal conductance κ_{el}, the Seebeck's coefficient S and the electrical conductance σ as a function of the density of carriers and for transport along the **a** and **b** directions of the unit cell.

Analysing the results [see Fig. 3 panes (a), (c), and (e)], we conclude that in the CRT, electronic transport shows a strong anisotropy with electron flow along **b** favored with respect to a flow along **a**. The situation is different when we consider hole transport [see Fig. 3 panes (b), (d), and (f)], in which case the transport coefficients do not show any particularly strong anisotropy, although transport along **a** is clearly favored. Interestingly, the Seebeck's coefficient is similar in all cases (notwithstanding the change of sign due to the opposite charges). As shown in Fig. S1 in the Supplemental Material [34], the density of the valence and conduction states at the Γ point shows different behaviors. Electron conduction appears limited along **a** direction, as the electrons are localized. Hole conduction is favored along the same direction since the valence state appears more diffusing in the unit cell. The opposite applies for the conduction band, where electron transport is favored. The same analysis shows that the electron thermal conductance is larger in the **b** direction. Indeed, the lattice thermal conductivity shows a significant anisotropy along the **a** and **b** directions. This can be justified through a purely geometrical argument, by counting the different number of bonds that each Ti atom forms with the S atoms along the two directions, as discussed in Ref. [35].

The situation is changed essentially when we consider the EPA approximation. In Fig. 4 we report the same transport coefficients calculated in the EPA scheme. EPA takes into account better the dependence of the scattering time on energy and thus should provide a more accurate evaluation of the transport coefficients. The first notable difference is that the strong anisotropy detected for the electron transport in the CRT is now suppressed. Although electron transport in the along **b** is still favored, the conductances for both axes have a similar order of magnitude. Also, for the hole transport, the two directions are essentially equivalent. Again the

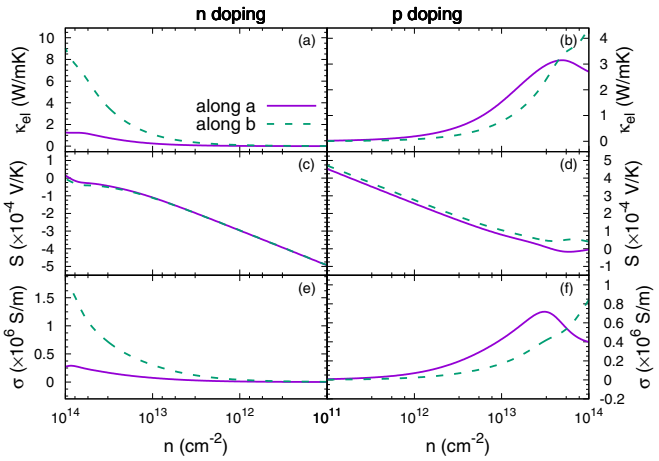

FIG. 4. Electron and hole transport coefficients for the monolayer TiS_3 evaluated in the EPA approximation. Panes (a) and (b) thermal conductance κ_{el} along different direction and doping, respectively. Panes (c) and (d) the Seebeck's coefficient S along different direction and doping, respectively. Panes (e) and (f) the electrical conductance σ along different direction and doping, respectively.

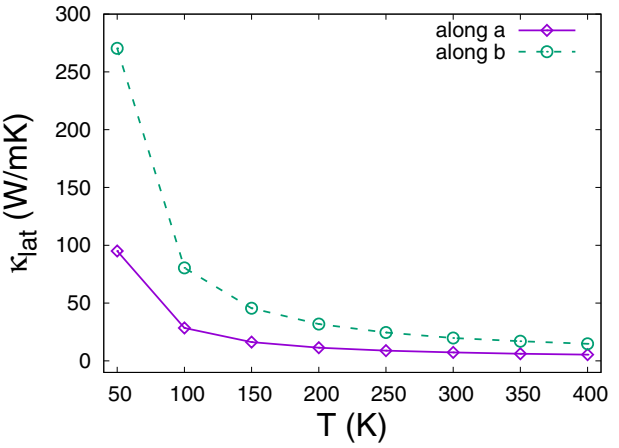

FIG. 5. Thermal conductance for the monolayer TiS_3 as function of temperature along the **a** and **b** axis.

Seebeck's coefficient appears insensitive to the direction of transport and the carrier charges.

We have calculated the same quantities at different temperatures and found a similar behavior of the transport coefficients. The CRT keeps pointing at a strong anisotropy in the transport coefficients, with a strongly favored flow along the **b** axis. On the other hand, the EPA offers a more balanced description, where the flow along b is still preferential, especially for electrons, but with conductances similar to those of a flow along the **a** axis.

We can summarize our results by looking at the figure of merit, ZT, for thermoelectric energy conversion. As seen in Eq. (2), to evaluate this coefficient, we need not only the electron/hole transport coefficients but also the phonon thermal conductance. In our case, we have calculated κ_{lat} through the phonopy code that takes the output of Quantum Espresso to evaluate the phonon transport by solving a linearized Boltzmann equation. The results of our calculations are reported in Fig. 5, where again the anisotropy in the transport coefficient is also confirmed for the phonons [36]. The lattice thermal conductivity is in good agreement with that reported in Ref. [7] as shown in Fig. S3 in the Supplemental Material [34].

In Fig. 6, we report ZT as a function of temperature and carrier concentration along different directions for transport (upper part along b and lower part along a). We see that the CRT approximation suggests that this material can be an excellent n-type candidate for thermoelectric applications, primarily when operated with a flow along the **b** axis and already at room temperature, we have a ZT of about 3 for n-doping of 10^{12} electrons per cm^2. Indeed, our results for the CRT approximation are in overall good agreement with those reported in Ref. [7] and within the error typical of using different codes and pseudopotentials, as one can appreciate by comparing Fig. S2 in the Supplemental Material [34] with those in Ref. [7]. The EPA reconsiders this conclusion and suggests that TiS_3 is still an attractive candidate as a p-type thermoelectric converter, although the overall figure of merit is strongly reduced. Indeed, we have to point out that this figure of merit has been obtained in ideal conditions without taking into account the presence of impurities or, more importantly, vacancies. For example, it is well known that TiS_3 is an S-poor atmosphere, eject S atoms creating vacancies that could then be closed in an S-rich atmosphere. These vacancies create extra states inside the band gap, thus facilitating transport [3]. To further investigate the nature of TiS_3 as a thermoelectric material, we looked at the bulk structure. Indeed, we know from experience that the transport properties of two- and three-layer TiS_3 are similar to the monolayer, and thus we do not expect any improvement. In Fig. 7, we report ZT for different carrier concentrations and temperature along the 3 axes of the unit cell. Overall, ZT along a and b is similar to that for the monolayer (compare with Fig. 6). On the other hand, ZT is larger along the c direction for the n doping. A way to understand this is to look at the lattice thermal conductance κ_{lat}.

In Fig. 8, we plot the lattice thermal conductance as a function of temperature along the 3 unit-cell axis. As expected, the thermal transport is strongly suppressed along the **c** axis due to the weak vdW bonds in this direction. On the other hand, the lattice thermal conductance is significantly larger in the in-plane directions due to the covalent bonds in the atomic structure. We find a strong in-plane anisotropy ratio (κ_b/κ_a) for the lattice thermal conductance of around 2 at 300 K, which agrees well with both experimental results [35]. A similar analysis can be performed for the other transport coefficients. Both the electrical and the thermal conductance are reduced in the **c** axis, while the Seebeck's coefficient shows a similar value in the range of carrier densities investigated here. Therefore, the increased ZT along the **c** axis stems from the balance between the reduced electrical conductance and the reduced lattice thermal conductance. Finally, the thermal conductivity is generally larger for the monolayer than the bulk as one can appreciate by comparing Fig. 5 and Fig. 8. This dissimilarity stems from the different velocity distributions and scattering lengths of the phonons modes, as it can be

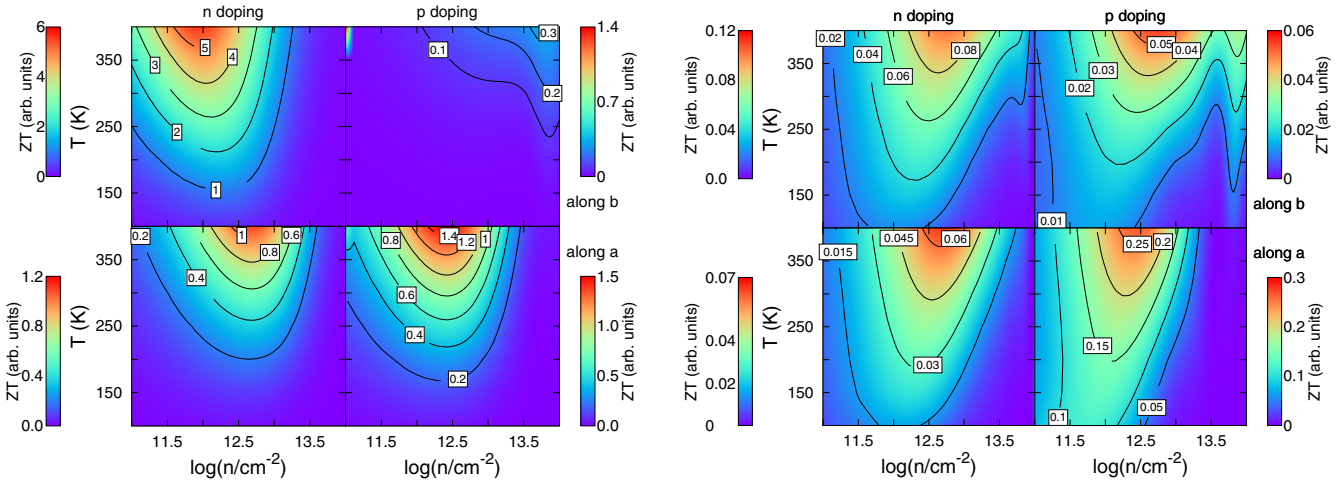

FIG. 6. Contour plot of ZT for monolayer TiS_3 evaluated in the (a) CRT approximation and (b) EPA as a function of carrier concentration and temperature. For both figures, in the upper part, the transport takes place along the **b** axis and in the bottom along **a**. The left panes refer to the material extrinsically doped with electron; in the right panes, doped with holes. Notice the different scale of the color-bar in the (a) and (b) sets of plots.

appreciated in Figs. S4 and S5 of the Supplemental Material [34].

IV. CONCLUSIONS

In conclusion, we have investigated the lattice and electron thermal transport for a prototype two-dimensional material, namely TiS_3. This material has been investigated for its potential range of application, spanning optical and electrical applications. Here, we looked at its potential as thermoelectric material. To pursue this investigation, we use a recently proposed technique to estimate the electron relaxation time from first-principle calculations. We show that the so-called EPA can capture the behavior of τ with the electron energy, especially when compared with the constant relaxation time approximation, which completely neglects the energy dependence of the relaxation time. We compare the EPA with the more accurate EPW and show overall good agreement. We expect that the correction to the relaxation time we have pointed out here is present and significant also for the whole family of 2D materials.

We found that the exceptional thermoelectric properties suggested for this material stem principally from the poor estimate of the relaxation time. We show indeed that the shortest relaxation time strongly suppresses the overall figure of merit, especially in the case of the monolayer. Bulk TiS_3 shows

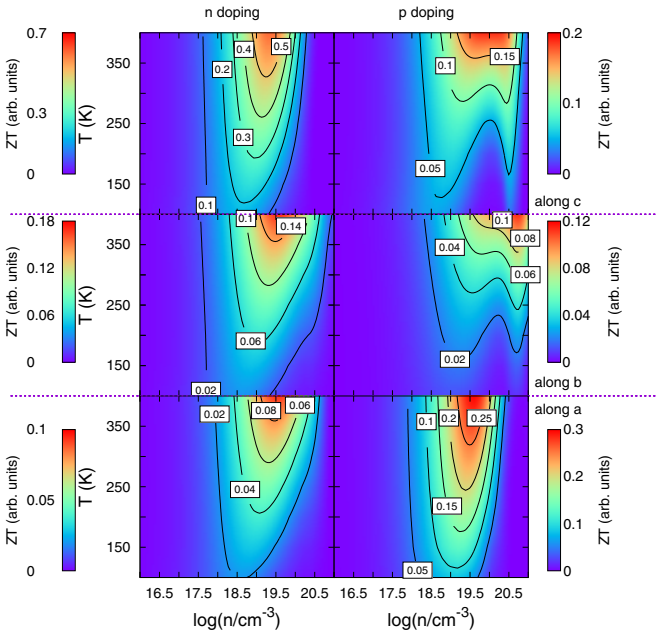

FIG. 7. Contour plot of ZT for bulk TiS_3 evaluated in the EPA as a function of carrier concentration and temperature. In the upper part, the transport takes place along the **c** axis, in the middle along **b**, and in the bottom along **a**. The left panes refer to the material extrinsically doped with electron; in the right panes, doped with holes.

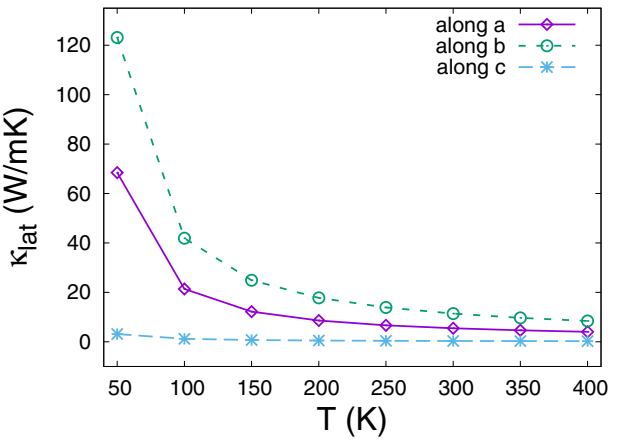

FIG. 8. The lattice thermal conductance for bulk TiS_3 for different directions as a function of temperature.

good thermoelectric performance, even more considering that we have investigated the pristine material where we made no effort to suppress the thermal conductance or increase the electron transport by doping. Indeed, it is known that TiS_3 can self-dope by losing S atoms in an S-poor atmosphere, thus increasing the electrical conductivity. Further studies on this direction are currently underway.

V. COMPUTATIONAL DETAILS

A. Ground state calculations

The electronic, structural, and vibrational properties of monolayer (ML) and bulk TiS_3 have been evaluated through density functional theory (DFT) and density functional perturbation theory calculations using the Quantum ESPRESSO code [37]. For both Ti and S, the electron exchange-correlation potential is evaluated within the generalized gradient approximation throughout the Perdew–Burke–Ernzerhof's functional. We have used the "GBRV" ultrasoft pseudopotential library that has been optimized for use in high-throughput DFT calculations [38]. By starting from the experimental parameters for the unit cell [3], and the spectroscopic atomic configuration [15], we have optimized the atomic positions with a residual force after relaxation of 0.001 a.u. The kinetic energy cutoff for the basis set is put at 120 Ry, while the cutoff for the charge density is 700 Ry. In the sampling of the Brillouin zone for the bulk material, we used a **k**-point mesh of $6\times6\times6$ (for ML, $10\times10\times1$). The chosen parameters ensure a convergence of the DFT band gap within an accuracy of around 0.01 eV. A semi-empirical GGA-type density functional has been used to incorporate vdW corrections in the bulk calculations [39,40]. In Fig. 1, we report the atomic structure of TiS_3 projected along the **a** axis after the atomic relaxation to reduce the residual forces. Weak vdW forces bind the structure along the **c** axis, and it is thus easily exfoliated to produce a monolayer sample [3]. The unit cell contains 8 atoms, 2 Ti and 6 S, as shown in Fig. 1.

B. Electron transport coefficients and relaxation time

BoltzTraP [41] has been used to calculate the electronic conductivity within the constant relaxation time (CRT) approximation by solving the semiclassical BTE. As DFT tends to underestimate the band gap, we have opened up the gap with a rigid shift of the conduction bands to the more realistic GW gap of around 1.1 eV for all transport calculation [3,42]. For the CRT approximation results, the relaxation time obtained within the deformation potential theory has been used [7]. To go beyond the simple CRT approximation, we have utilized the EPA approximation to calculate the energy-dependent relaxation time $\tau(\omega)$, which then enters the solution of the BTE. Using the fully relaxed structure, we performed e-p calculations with $10\times10\times1$ k points and $4\times4\times1$ q points for the monolayer case, while we employed $8\times8\times8$ k-point and $3\times3\times3$ q-point samplings for the bulk. The dynamical matrix was then fed into EPA to obtain an average e-p dynamical matrix. This average matrix was then fed into a modified BoltzTraP code along with the other required parameters to calculate the carrier relaxation time. To test the validity of the EPA results we have calculated the relaxation time for the ML (shown in Fig. 2) by directly solving Eq. (1) with then EPW code by interpolating from a coarse $4\times4\times1$ q-points grid to a dense 512×512 grid [32,33].

C. Lattice thermal transport

The lattice thermal conductivity κ_{lat} has been calculated by using the finite displacement methods as implemented in Phono3py [43,44]. For this, the second- and third-order inter-atomic force constants were calculated by creating a $2\times2\times2$ supercell (ML :$3\times3\times1$) in Quantum Espresso with a grid of $4\times4\times4$ k points (ML: $5\times5\times1$) and keeping the other parameter the same. The lattice thermal conductivity was obtained by solving the linearized phonon Boltzmann transport equation with a grid of $10\times10\times10$ q points (for ML $40\times40\times1$).

ACKNOWLEDGMENTS

R.D'A. acknowledges support from the "Grupos Consolidados UPV/EHU del Gobierno Vasco" (Eusko Jaurlaritza Grant No. IT1249-19), the Red Consolider of Spanish Government "TowTherm" (Ministerio de Economia y Competitividad Grant No. ENE2017-90743-REDC) and Grant QuEST (Grant No. PID2020-112811GB-I00) funded by Ministerio de Ciencia y Investigacion/Agencia Estatal de Investigacion 10.13039/501100011033 and by "ERDF A way of making Europe" by the European Union. R.B. acknowledges funding from the European Union's Horizon 2020 research and innovation program under the Marie Skłodowska-Curie Grant Agreement No. 793318.

[1] K. S. Novoselov, A. K. Geim, S. V. Morozov, D. Jiang, Y. Zhang, S. V. Dubonos, I. V. Grigorieva, and A. A. Firsov, Electric field effect in atomically thin carbon films, Science **306**, 666 (2004).

[2] A. Chaves, J. G. Azadani, H. Alsalman, D. R. da Costa, R. Frisenda, A. J. Chaves, S. H. Song, Y. D. Kim, D. He, J. Zhou *et al.*, Bandgap engineering of two-dimensional semiconductor materials, npj 2D Mater. Appl. **4**, 29 (2020).

[3] J. O. Island, M. Barawi, R. Biele, A. Almazán, J. M. Clamagirand, J. R. Ares, C. Sánchez, H. S. J. van der Zant, J. V. Álvarez, R. D'Agosta *et al.*, TiS_3 transistors with tailored morphology and electrical properties, Adv. Mater. **27**, 2595 (2015).

[4] J. O. Island, R. Biele, M. Barawi, J. M. Clamagirand, J. R. Ares, C. Sánchez, H. S. J. van der Zant, I. J. Ferrer, R. D'Agosta, and A. Castellanos-Gomez, Titanium trisulfide (TiS_3): A 2D semiconductor with quasi-1D optical and electronic properties, Sci. Rep. **6**, 22214 (2016).

[5] R. Biele, E. Flores, J. R. Ares, C. Sanchez, I. J. Ferrer, G. Rubio-Bollinger, A. Castellanos-Gomez, and R. D'Agosta, Strain-induced band gap engineering in layered TiS_3, Nano Res. **11**, 225 (2018).

[6] F. Saiz and R. Rurali, Strain engineering of the electronic and thermoelectric properties of titanium trisulphide monolayers, Nano Ex. **1**, 010026 (2020).

[7] J. Zhang, X. Liu, Y. Wen, L. Shi, R. Chen, H. Liu, and B. Shan, Titanium trisulfide monolayer as a potential thermoelectric material: A first-principles-based Boltzmann transport study, ACS Appl. Mater. Interfaces **9**, 2509 (2017).

[8] Z. Zhou, H. Liu, D. Fan, G. Cao, and C. Sheng, High thermoelectric performance originating from the grooved bands in the $ZrSe_3$ monolayer, ACS Appl. Mater. Interfaces **10**, 37031 (2018).

[9] J. Dai and X. C. Zeng, Titanium trisulfide monolayer: Theoretical prediction of a new direct-gap semiconductor with high and anisotropic carrier mobility, Angew. Chem., Int. Ed. **54**, 7572 (2015).

[10] I. Ferrer, J. Ares, J. Clamagirand, M. Barawi, and C. Sánchez, Optical properties of titanium trisulphide (TiS_3) thin films, Thin Solid Films **535**, 398 (2013).

[11] Y.-Q. Wang, X. Wu, Y.-F. Ge, Y.-L. Wang, H. Guo, Y. Shao, T. Lei, C. Liu, J.-O. Wang, S.-Y. Zhu *et al.*, Tunable electronic structures in wrinkled 2D transition-metal-trichalcogenide (TMT) $HfTe_3$ films, Adv. Electron. Mater. **2**, 1600324 (2016).

[12] J. Kang and L.-W. Wang, Robust band gap of TiS_3 nanofilms, Phys. Chem. Chem. Phys. **18**, 14805 (2016).

[13] F. Iyikanat, R. T. Senger, F. M. Peeters, and H. Sahin, Quantum-transport characteristics of a p-n junction on single-layer TiS_3, ChemPhysChem **17**, 3985 (2016).

[14] F. Iyikanat, H. Sahin, R. T. Senger, and F. M. Peeters, Vacancy formation and oxidation characteristics of single layer TiS_3, J. Phys. Chem. C **119**, 10709 (2015).

[15] S. Furuseth, L. Brattas, and A. Kjejshus, On the crystal structures of TiS_3, ZrS_3, $ZrSe_3$, $ZrTe_3$, HfS_3, and $HfSe_3$, Acta Chem. Scand. **29a**, 623 (1975).

[16] R. Fei, A. Faghaninia, R. Soklaski, J. A. Yan, C. Lo, and L. Yang, Enhanced thermoelectric efficiency via orthogonal electrical and thermal conductances in phosphorene, Nano Lett. **14**, 6393 (2014).

[17] B. Liao, J. Zhou, B. Qiu, M. S. Dresselhaus, and G. Chen, *Ab initio* study of electron-phonon interaction in phosphorene, Phys. Rev. B **91**, 235419 (2015).

[18] G. Gaddemane, W. G. Vandenberghe, M. L. Van de Put, S. Chen, S. Tiwari, E. Chen, and M. V. Fischetti, Theoretical studies of electronic transport in monolayer and bilayer phosphorene: A critical overview, Phys. Rev. B **98**, 115416 (2018).

[19] K. Momma and F. Izumi, VESTA 3 for three-dimensional visualization of crystal, volumetric and morphology data, J. Appl. Crystallogr. **44**, 1272 (2011).

[20] G. Samsonidze and B. Kozinsky, Accelerated screening of thermoelectric materials by first-principles computations of electron-phonon scattering, Adv. Energy Mater. **8**, 1800246 (2018).

[21] A. M. Ganose, J. Park, A. Faghaninia, R. Woods-Robinson, K. A. Persson, and A. Jain, Efficient calculation of carrier scattering rates from first principles, Nat. Commun. **12**, 2222 (2021).

[22] F. Giustino, Electron-phonon interactions from first principles, Rev. Mod. Phys. **89**, 015003 (2017).

[23] G. S. Nolas, J. Sharp, and H. J. Goldsmid, *Thermoelectrics: Basic Principles and New Materials Developments*, Springer Series in Material Science, Vol. 45 (Springer Verlag, Berlin, 2001).

[24] O. Caballero-Calero and R. D'Agosta, Review–towards the next generation of thermoelectric materials: Tailoring electronic and phononic properties of nanomaterials, ECS J. Solid State Sci. Technol. **6**, N3065 (2017).

[25] R. D'Agosta, Towards a dynamical approach to the calculation of the figure of merit of thermoelectric nanoscale devices, Phys. Chem. Chem. Phys. **15**, 1758 (2013).

[26] R. Biele and R. D'Agosta, Beyond the state of the art: Novel approaches for thermal and electrical transport in nanoscale devices, Entropy **21**, 752 (2019).

[27] K. Kaasbjerg, K. S. Thygesen, and K. W. Jacobsen, Phonon-limited mobility in *n*-type single-layer MoS_2 from first principles, Phys. Rev. B **85**, 115317 (2012).

[28] F. Murphy-Armando and S. Fahy, First-principles calculation of carrier-phonon scattering in *n*-type $Si_{1-x}Ge_x$ alloys, Phys. Rev. B **78**, 035202 (2008).

[29] F. Murphy-Armando, G. Fagas, and J. C. Greer, Deformation potentials and electron-phonon coupling in silicon nanowires, Nano Lett. **10**, 869 (2010).

[30] B. Xu and M. J. Verstraete, First Principles Explanation of the Positive Seebeck Coefficient of Lithium, Phys. Rev. Lett. **112**, 196603 (2014).

[31] S. Y. Savrasov and D. Y. Savrasov, Electron-phonon interactions and related physical properties of metals from linear-response theory, Phys. Rev. B **54**, 16487 (1996).

[32] S. Poncé, E. Margine, C. Verdi, and F. Giustino, EPW: Electron–phonon coupling, transport and superconducting properties using maximally localized Wannier functions, Comput. Phys. Commun. **209**, 116 (2016).

[33] S. Poncé, E. R. Margine, and F. Giustino, Towards predictive many-body calculations of phonon-limited carrier mobilities in semiconductors, Phys. Rev. B **97**, 121201(R) (2018).

[34] See Supplemental Material at http://link.aps.org/supplemental/10.1103/PhysRevMaterials.6.014004 for an explanation of the electronic anisotropy, difference between bulk and monolayer thermal transport properties, and comparison of the figure of merit and lattice conductance with the literature.

[35] H. Liu, X. Yu, K. Wu, Y. Gao, S. Tongay, A. Javey, L. Chen, J. Hong, and J. Wu, Extreme in-plane thermal conductivity anisotropy in titanium trisulfide caused by heat-carrying optical phonons, Nano Lett. **20**, 5221 (2020).

[36] For the monolayer, we have normalized κ_{lat} by the numerical factor 20.28/8.72, i.e., the ratio of the height of unit cell used in the calculation and the estimated thickness of the monolayer. Indeed, in Quantum Espresso, we need to add a consistent amount of vacuum to avoid interaction within the replica induced by periodic boundary conditions.

[37] P. Giannozzi, S. Baroni, N. Bonini, M. Calandra, R. Car, C. Cavazzoni, D. Ceresoli, G. L. Chiarotti, M. Cococcioni, I. Dabo *et al.*, QUANTUM ESPRESSO: A modular and open-source software project for quantum simulations of materials, J. Phys.: Condens. Matter **21**, 395502 (2009).

[38] K. F. Garrity, J. W. Bennett, K. M. Rabe, and D. Vanderbilt, Pseudopotentials for high-throughput DFT calculations, Comput. Mater. Sci. **81**, 446 (2014).

[39] S. Grimme, Semiempirical GGA-type density functional constructed with a long-range dispersion correction, J. Comput. Chem. **27**, 1787 (2006).

[40] V. Barone, M. Casarin, D. Forrer, M. Pavone, M. Sambi, and A. Vittadini, Role and effective treatment of dispersive forces in materials: Polyethylene and graphite crystals as test cases, J. Comput. Chem. **30**, 934 (2009).

[41] G. K. Madsen and D. J. Singh, BoltzTraP. A code for calculating band-structure dependent quantities, Comput. Phys. Commun. **175**, 67 (2006).

[42] F. Ghasemi, R. Frisenda, E. Flores, N. Papadopoulos, R. Biele, D. Perez de Lara, H. S. J. van der Zant, K. Watanabe, T. Taniguchi, R. D'Agosta *et al.*, Tunable photodetectors via in situ thermal conversion of TiS_3 to TiO_2, Nanomaterials **10**, 711 (2020).

[43] A. Togo, L. Chaput, and I. Tanaka, Distributions of phonon lifetimes in Brillouin zones, Phys. Rev. B **91**, 094306 (2015).

[44] K. Mizokami, A. Togo, and I. Tanaka, Lattice thermal conductivities of two Si_2 polymorphs by first-principles calculations and the phonon Boltzmann transport equation, Phys. Rev. B **97**, 224306 (2018).